

Wet to Dry Controls Lanthanide Scandate Synthesis

Emily P. Greenstein,* Kenneth R. Poeppelmeier, and Laurence D. Marks



Cite This: <https://doi.org/10.1021/acs.inorgchem.2c04107>



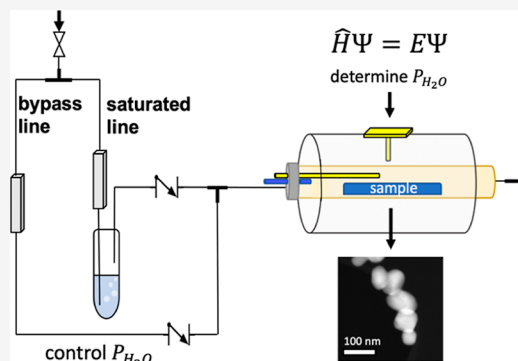
Read Online

ACCESS |

Metrics & More

Article Recommendations

ABSTRACT: The choice of temperature and gas conditions used in a water pressure-controlled reactor is guided by density functional theory (DFT) to synthesize nearly phase-pure lanthanide scandate nanoparticles (LnScO_3 , Ln = La, Nd, Sm, Gd). In this synthetic method, low water-vapor partial pressures, well below water's gas liquidus, inhibit particle growth, while an excess of water vapor results in undesired rare-earth hydroxide and oxyhydroxide secondary phases. The optimal humidity for high-purity LnScO_3 particle synthesis is shown to vary with the lanthanide; DFT is used to calculate the thermodynamics of secondary phase formation for each lanthanide tested such that the role of water vapor may be quantified and used to maintain phase purity (greater than 96 mol %) across the series. The combination of thermodynamic calculation and experimental confirmation with this pressure-controlled reactor provides an opportunity to explore analogous syntheses of other inorganic perovskite nanoparticles.



INTRODUCTION

Hydrothermal synthesis is often an effective and accessible route to producing oxide nanoparticles;^{1,2} however, synthetic conditions greatly impact the product and its physical properties, often in ways that are difficult to quantify.^{2–4} A material's precursors, and their sensitivities to the environment, complicate our ability to predict what occurs inside an autoclave or other reactor. To predict synthetic conditions, one must understand the thermodynamic stability of the phase one wishes to synthesize. In the past, this has been done by formulating thermodynamic metrics for compound “formability” under various conditions, for example, a thermodynamically derived maximum driving force⁵ or an activity coefficient model for nonideal solutions which would be present under hydrothermal conditions.⁶ More recently, machine learning has been used to predict perovskite synthesis with training data sets based on experimentally observed perovskite syntheses⁷ and even under the synthetic conditions used in unsuccessful syntheses.⁸

Lanthanide scandates (LnScO_3) provide a particular challenge in the realm of predictive material synthesis. While LnScO_3 nanoparticles may find potential uses in a wide array of applications owing to their large optical band gap,⁹ potential for morphological control,¹⁰ and interesting surface properties,¹¹ the thermodynamics of lanthanide perovskite formation is still not completely understood.^{12,13} Each LnScO_3 has a different lattice parameter while retaining the bulk $Pbnm$ orthorhombic perovskite structure.^{14–16} Across the LnScO_3 series, they also share similar electronic structures and surface terminations.^{17,18} However, while it is common to extrapolate

or assume linear trends across the lanthanide series because of linearly changing properties like Ln^{3+} cation radius or Ln–O bond length,^{19,20} evidence suggests that the Ln^{3+} electronic structure^{21–25} and resulting properties such as Lewis acidity^{11,26} do not trend linearly with Ln. Thus, without a robust understanding of the thermodynamics of their formation, it is difficult to predict how synthetic conditions for LnScO_3 will vary as the lanthanide is changed.

In previous work, LnScO_3 of four different lanthanides (Ln = La, Nd, Sm, and Gd) was synthesized hydrothermally from a mixed-cation hydrogel precursor,²⁷ but the methods used often resulted in significant fractions of ScOOH , LnOOH , and $\text{Ln}(\text{OH})_3$ rather than the desired LnScO_3 perovskite phase. In earlier work, we hypothesized that this varied presence of hydroxide and oxyhydroxide phases was due to an uncontrolled and often relatively high concentration of water vapor in the synthesis environment.²⁷ For instance, considering the reaction



Received: November 21, 2022

Excess water will drive this reaction to the right, suggesting that the water-vapor partial pressure must be controlled. Here, this hypothesis is proved rigorously using both density functional theory (DFT) and experiment, and consistent high-purity LnScO_3 synthesis is achieved. We approach this challenge experimentally with a hydrosaua method, which uses an open environment with a lower humidity than hydrothermal or other hydrosaua approaches.¹⁰ Because slight changes in the chemical potential of water can result in a wide range of LnScO_3 phase purity, and because—as we will demonstrate—the optimal chemical potential of water varies with Ln, modifications to the hydrosaua method are required.

There are several factors complicating the purely experiment-based understanding of LnScO_3 formation. First, given its sensitivity to water content, the hydrogel precursor is not conducive to common in situ X-ray diffraction techniques; sample holders frequently used for in situ XRD experiments such as capillary tubes alter the gel's water exposure and drying rate by increasing the gel packing density and the area exposed to flowing gas. Furthermore, assumptions that hold for in situ studies of other perovskite materials or even hydrothermally synthesized $\text{Ln}(\text{OH})_3$ may not hold for the LnScO_3 material system in a hydrosaua environment^{12,13,28} as the phase diagrams of the $\text{Ln}_2\text{O}_3\text{--H}_2\text{O}$ system are known to vary greatly for various Ln.^{12,29} For example, for some lanthanides such as La, Nd, and Sm, conversion from $\text{Ln}(\text{OH})_3$ to LnOOH occurs at high temperatures, and in fact, LnOOH may be required as an intermediate in the formation of some Ln-containing oxides from $\text{Ln}(\text{OH})_3$,^{13,30} while for other lanthanides such as Dy, the LnOOH structure is rarely observed.^{12,30} Lastly, as alluded to previously, the electronic structure and other properties do not necessarily trend linearly across the lanthanide series. It is therefore difficult to determine experimentally how the thermodynamics of the $\text{Ln}_2\text{O}_3/\text{H}_2\text{O}$ system will impact LnScO_3 formation and how that impact can be exploited in designing its synthesis.

A modeling approach provides another path to determine the thermodynamics of the involved hydroxide, oxyhydroxide, and oxide phases; however, this route also has problems to overcome, namely, the handling of the 4f electrons in LnScO_3 . Previous studies have treated 4f systems using generalized gradient approximation and a Hubbard + U .³¹ DFT + U methods place 4f states far below the valence band maximum, where they may be wrongly treated as core-like states.¹⁷ In fact, experimental studies of the valence band structure of LnScO_3 by X-ray photoelectron spectroscopy (XPS) show that Ln 4f electrons in these materials are often actually valence-active and should not be treated as core states.^{17,21–25,32}

To expand on this, as it will become important later, XPS and other photoelectron spectroscopy techniques primarily probe the occupied density of states,³³ with results for the valence region yielding spectra such as those in Figure 1.^{21–24} This technique is well suited to accurate measurements of the electronic structure even in correlated electron systems because, at the incident X-ray energies typically used for XPS (1253.6–9251.7 eV),³³ Ln 4f photoionization cross sections are notably higher than the cross sections of other states contributing to the valence band,³⁴ namely, Sc 3d and O 2p states.^{21–25,31} Thus, differences between XPS valence spectra of various LnScO_3 depict Ln 4f contributions.

From the XPS valence spectra, we see that in various LnScO_3 , Ln 4f states reside close to or in some cases at the

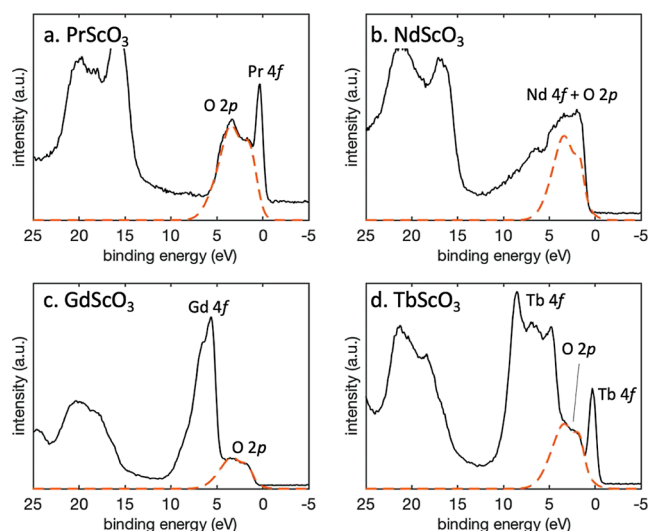


Figure 1. XPS valence spectra of four LnScO_3 (110) bulk crystals: (a) PrScO_3 , (b) NdScO_3 , (c) GdScO_3 , and (d) TbScO_3 . As a guide to the eye, the approximate magnitude of the O 2p contribution is marked by the dashed red lines. O 2p states maintain approximately the same magnitude and position for each LnScO_3 , while the Ln 4f peak magnitude and position vary. The X-ray source was monochromatic Al $K\alpha$ radiation with an energy of 1486.6 eV; note that at this energy, Ln 4f photoionization cross sections are notably greater than other valence band contributors.³⁴ The features from 15–25 eV correspond to the Ln 5p doublet and O 2s peaks, which also remain relatively constant for each LnScO_3 . Reproduced with modifications of the scale and labeling from *Surf. Sci. Spectra* 21, 131–164 (2014), with the permission of AIP Publishing.^{21–24}

valence band maximum^{21–25} and should not be treated as core-like states via DFT + U methods.¹⁷ For example, in the experimental XPS valence spectrum for GdScO_3 shown in Figure 1c, there is a clear distinction between O 2p states near the valence band edge, where the binding energy is at or just above 0 eV and the Gd 4f states which are farther down but still present at the bottom of the valence band. The magnitude and position of O 2p peaks in LnScO_3 remain approximately constant regardless of the lanthanide, as represented by the dashed red lines in Figure 1. In contrast, the Ln 4f peak resides much closer to the valence band edge in NdScO_3 or PrScO_3 , and TbScO_3 has seven states quite low but one right at the valence band edge. Herein, we accurately handle the Ln 4f states by avoiding DFT + U methods and instead using an on-site hybrid DFT approach,³⁵ which is described further in the next section and has previously shown very good agreement between experimental XPS valence spectra and simulated spectra for several LnScO_3 .¹⁷

In this paper, DFT modeling of the thermodynamics of the $\text{Ln}_2\text{O}_3/\text{H}_2\text{O}$ material system is used to guide the choice of water-vapor partial pressure in the LnScO_3 hydrosaua synthesis. Our understanding of the thermodynamics of LnScO_3 formation across the lanthanide series, coupled with our modified hydrosaua synthesis method, enables us to generate nearly phase-pure LnScO_3 for multiple lanthanides.

EXPERIMENTAL SECTION

To produce LnScO_3 nanoparticles, an equimolar solution of lanthanide and scandium ions was prepared by dissolving 4 mmol each of Ln_2O_3 (Ln = La, Nd, Sm, Gd) and Sc_2O_3 in 20 mL of 15.8 N nitric acid stirred at 90 °C. After the liquid evaporated, the resulting nitrate precursor was dissolved in 20 mL of deionized water and then

added dropwise to 50 mL of 10 M NaOH in an ice bath to precipitate a mixed-cation hydroxide hydrogel, the precursor for LnScO₃ growth. The hydrogel was isolated via a centrifuge at 4500 rpm for seven min and washed three times with deionized water, resulting in 5–10 g of gel that was then transferred to the furnace which is described below. To generate a humid environment, argon gas was flowed through a water bubbler upstream of the furnace; we will call this setup the “one-line” method for its single gas inlet line. The gel was then calcined in the furnace using a two-step treatment: a high-temperature step at 450 °C for 2 days and then a low-temperature step at 300 °C for 1 day.¹⁰ The product was rinsed with deionized water and centrifuged several times, and the roughly 2–5 g of powder that was retrieved was then put into a drying oven at 110 °C overnight.

As previously indicated, water-vapor partial pressure must be controlled precisely to attain highly phase-pure LnScO₃. In addition, the optimal water chemical potential for each of the two synthetic stages may be different, as will be discussed later. To control these factors, a “two-line” reactor with variable water chemical potential was used as shown in Figure 2.

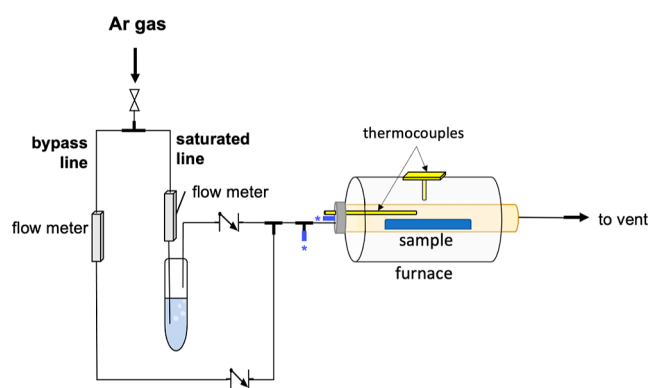


Figure 2. Schematic of the hydrosauuna tube furnace reactor including the two-line mechanism for controlling water-vapor partial pressure. The bypass line provides dry argon gas, while the saturated line passes the gas through a bubbler filled with deionized water. Blue inlet lines marked with an asterisk (*) indicate locations at which a hygrometer was placed to monitor humidity.

Variable-area flow meters allow for precise monitoring of argon gas flow rates through two lines: a saturated line passing through the water bubbler and a bypass line that remains dry. Adjusting the flow rates through each line allows for control of the partial pressure of water in the inlet gas stream, ranging from 0.1 to 20 torr; the latter is the saturation pressure of water in argon gas at room temperature. This pressure range can be calculated by gas laws for any similar system for which the volume is known; for the reactor described, these values were also confirmed by direct measurement of the relative humidity with a hygrometer placed upstream of the furnace (at the marked inlet locations) and use of the equation

$$\text{Relative humidity} = \frac{P_{\text{H}_2\text{O}}}{P_{\text{vap}}} \times 100\%$$

where P_{vap} is the vapor pressure of water at the appropriate temperature.

Powder X-ray diffraction (PXRD) was performed on a Rigaku Ultima diffractometer using a Cu ($\lambda = 1.54 \text{ \AA}$) source operated at 40 kV and 35 mA in the Bragg–Brentano geometry. To maintain high peak intensity, no monochromatization was done, and a $K\beta$ nickel filter was used; the $K\beta$ lines consequently do not appear at the diffraction peak intensities observed in these experiments. Secondary electron (SE) and high-angle annular dark field (HAADF) imaging for the overall nanoparticle morphology were performed on a Hitachi HD-2300 scanning transmission electron microscope operated at 200 kV. Simultaneous thermogravimetric analysis (TGA) and differential thermal analyses (DTA) measurements were performed on a Netzsch

Jupiter F3 Simultaneous Thermal Analysis system from room temperature to 550 °C and back at a rate of 10 °C min⁻¹ with an air flow of 50 mL min⁻¹.

DFT calculations were done with WIEN2k, an all-electron augmented plane wave + local orbital package.³⁶ The PBEsol functional³⁷ was used in an on-site hybrid approach, which applies an exact exchange hybrid correction on correlated electrons within the muffin tins which would otherwise be poorly described by conventional functionals.³⁵ Hybrid fractions of 0.38 and 0.50 were used for the Ln 4f and Ln 5d orbitals, respectively, previously shown to describe LnScO₃ accurately¹⁷ and confirmed via force minimization to describe the lanthanide oxides, hydroxides, and oxyhydroxides as well. Muffin-tin radii of 2.02, 1.2, and 0.5 Bohr were used for Ln, O, and H atoms, respectively, in the cases of LnOOH and Ln(OH)₃. In calculations of Ln₂O₃ and LnScO₃, a muffin-tin radius of 1.82 Bohr was used for Sc atoms, and the radius of O atoms was increased to 1.5 Bohr to accommodate the absence of short O–H bonds. The plane-wave expansion parameter RKMAX was 7.2 for all oxides and 3.0 for all hydroxides and oxyhydroxides. Calculations of LnScO₃ were done for a ferromagnetic model as the Néel temperatures for the lanthanide scandates are generally below 5 K,³¹ so the difference between ferromagnetic and antiferromagnetic ordering is negligible.

RESULTS

Hydrosauuna synthesis of LnScO₃ was done by calcining a mixed-cation hydroxide gel in a humid environment. The precursor gel material has the approximate formula LnSc(OH)₆ \cdot x H₂O. As determined from TGA and DTA, shown for one NdScO₃ synthesis in Figure 3, the number of coordinated

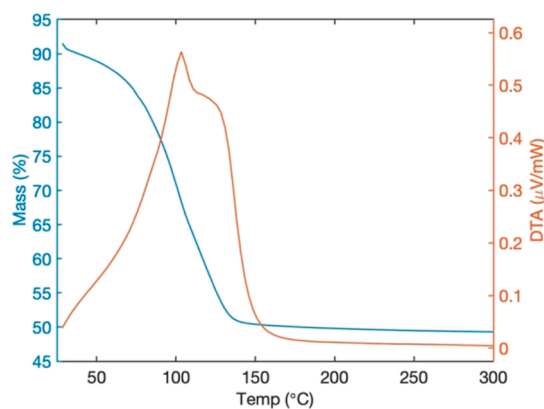


Figure 3. Simultaneous TGA (blue) and DTA (red) curves of the dehydration of the NdSc(OH)₆ \cdot x H₂O hydrogel to NdScO₃; the results shown indicate $x = 6$.

water molecules x is on average 6–8;²⁷ the results shown indicate a case where $x \sim 6$. Note that the initial drop in mass around room temperature was likely not due to water loss, but an artifact resulting from the relatively fast temperature ramp rate of 10 °C min⁻¹, chosen to replicate conditions in the hydrosauuna reactor during a synthesis. The gel material is about 50% water by mass, and hydrosauuna synthesis is therefore best conducted in an open system. In a closed system, water desorbing from the drying gel changes the chemical potential of water in a way that is difficult to measure and varies between syntheses with variations in the number of coordinated water molecules in the gel.

The hydrosauuna process can yield a variety of results, generating powders with 60–99 wt % LnScO₃ as determined from PXRD if the partial pressure of water in the flowing carrier gas is not controlled. We hypothesize that this range in product yield is attributed to environmental changes caused by

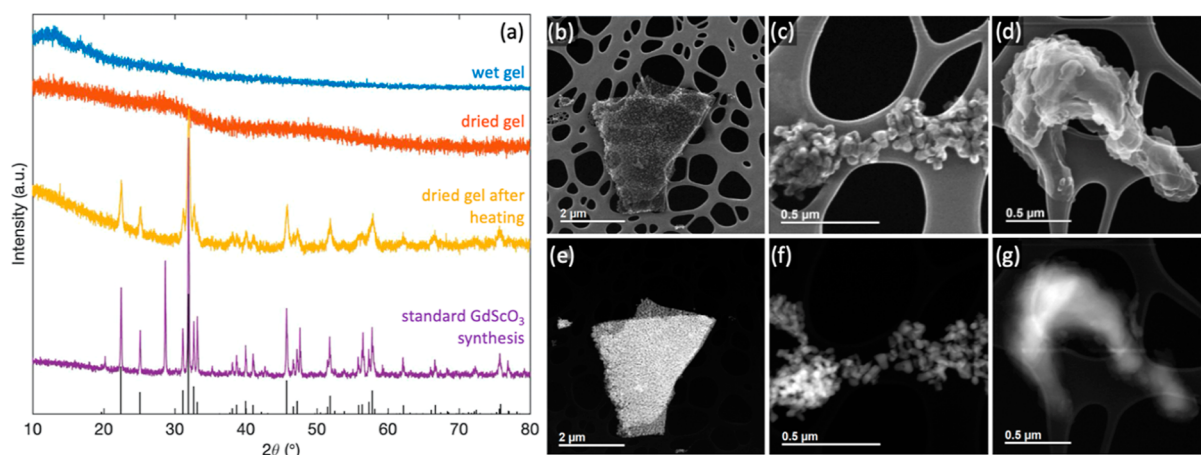


Figure 4. (a) PXRD patterns for the mixed-cation $\text{GdSc}(\text{OH})_6 \cdot x\text{H}_2\text{O}$ ($x \sim 6$) gel precursor (blue) as produced, (red) after drying in air at room temperature for 3 days, and (yellow) after calcining the air-dried gel in the one-line hydrosauuna reactor according to the established two-step procedure, compared to (purple) GdScO_3 resulting from a standard hydrosauuna synthesis directly from the wet gel. The calculated pattern for pure GdScO_3 , obtained from the crystal structure determined by Veličkov et al.,³⁸ is shown in black at the bottom. Broad peaks are indicative of amorphous material or small, nanoscale grains. (b–d) SE STEM and (e–g) corresponding HAADF STEM images of the powder resulting from this hydrosauuna synthesis of the predried gel.

unintentionally varied bubbler temperature or flow rates. To observe the effects of these unintentional changes, experiments were performed by taking advantage of the water in the gel itself to provide differing levels of humidity. First, a $\text{GdSc}(\text{OH})_6 \cdot x\text{H}_2\text{O}$ ($x \sim 6$) mixed-cation precursor gel was prepared according to the procedure described (see the Experimental Section). Then, instead of calcining the as-prepared wet gel using the previously defined method, in what we will henceforth refer to as a “standard” hydrosauuna synthesis, the gel was first dried in air at room temperature for 3 days. This dried gel was then calcined in the established one-line hydrosauuna method. PXRD and STEM results of this experiment are shown in Figure 4.

The inability to resolve sharp diffraction peaks in Figure 4a shows that the precursor gel is X-ray amorphous (i.e., small, nanoscale grains) and largely remains so after drying out at room temperature. Even so, nucleation of the perovskite GdScO_3 phase can still be identified after calcination in the hydrosauuna condition in the yellow pattern in Figure 4a, though the SE and corresponding HAADF STEM images in Figure 4b–g indicate that the resulting particles were very small, averaging below 10 nm in length or occasionally larger but without their expected well-faceted nanocuboid morphology, as in Figures 4d and g. Note that these particles typically display an orthorhombic shape with a long *c* axis; as these HAADF images are two-dimensional projections of the sample, particles that appear cuboidal are simply viewed along this long axis. The “length” is the measurement along this axis where it is visible. By comparing the PXRD pattern of the calcined dried gel to that of a standard GdScO_3 synthesis (i.e., calcined from wet gel) in Figure 4a, it can also be seen that the crystallite size was increased significantly by calcining the wet gel, notable by the narrower, sharper crystalline peaks. Notably, all hydroxide and oxyhydroxide phases are absent from the dried-gel PXRD pattern in Figure 4a, presumably because of the lack of excess water vapor but not from the standard synthesis pattern.

The chemical potential of water must therefore reach some value required to allow particle growth while remaining relatively low to minimize the formation of hydroxide and oxyhydroxide phases. This phenomenon can be observed

clearly in the case of NdScO_3 in Figure 5, which shows the boundaries within which lies some optimum water-vapor

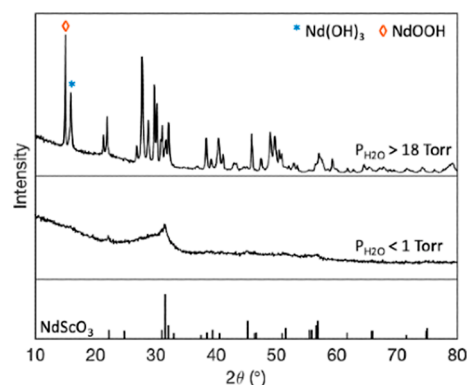


Figure 5. PXRD patterns of powder resulting from two NdScO_3 syntheses. The top pattern shows the presence of $\text{Nd}(\text{OH})_3$ and NdOOH in the case where water-vapor partial pressure is too high. The middle pattern shows an X-ray amorphous material in the case where water-vapor partial pressure is too low. The calculated pattern for NdScO_3 is shown at the bottom, obtained from the crystal structure of Veličkov et al.³⁸

partial pressure required to achieve crystalline, well-faceted NdScO_3 nanoparticles. A high water-vapor partial pressure yields undesired hydroxide and oxyhydroxide phases, while a low water-vapor partial pressure yields very small crystallites, leading to peak broadening and a nearly X-ray amorphous pattern. A two-line hydrosauuna reactor permits the precision required to control the water vapor pressure within these parameters.

We take two approaches to determine the optimal water-vapor partial pressure for each lanthanide: both calculations and experiment. From the theoretical side, the value of the optimal $P_{\text{H}_2\text{O}}$ depends on the thermodynamics of the formation of LnScO_3 , $\text{Ln}(\text{OH})_3$, and LnOOH from the starting materials, Sc_2O_3 and Ln_2O_3 . Since not all lanthanides readily form the LnOOH phase and properties such as Lewis acidity are not linear across the lanthanide series for Ln^{3+} or

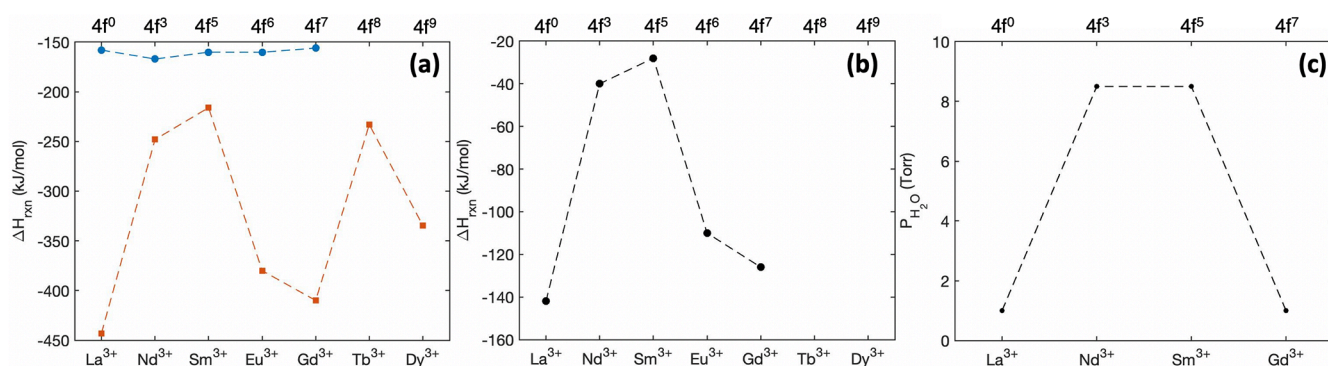


Figure 6. (a) Energy trends for the reactions $1/2\text{Ln}_2\text{O}_3 + 1/2\text{H}_2\text{O} \rightarrow \text{LnOOH}$ (blue circle) and $1/2\text{Ln}_2\text{O}_3 + 3/2\text{H}_2\text{O} \rightarrow \text{Ln}(\text{OH})_3$ (red square) for various lanthanides. (b) Energy trend for the reaction $\text{LnOOH} + \text{H}_2\text{O} \rightarrow \text{Ln}(\text{OH})_3$. (c) Water vapor pressure used to synthesize high-purity LnScO_3 . Lanthanides which are not shown (Tb and Dy) are those for which no experimental LnOOH structures were found.

LnScO_3 ,^{11,26} we should not assume linearity with Ln in these thermodynamics. The optimal $P_{\text{H}_2\text{O}}$ for LnScO_3 across the lanthanide series may vary according to some other calculable trend.

To establish this trend, DFT was used to calculate the formation energies of both LnOOH (eq 1) and $\text{Ln}(\text{OH})_3$ (eq 2) from Ln_2O_3 as a function of atomic number across the lanthanide series.

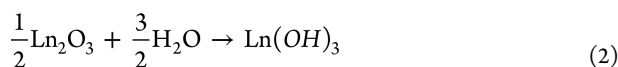
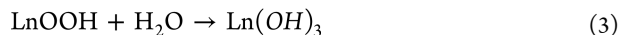


Figure 6a shows these energies. These results indicate that La and Gd have a stronger driving force to form $\text{Ln}(\text{OH})_3$ than Nd and Sm; previous work suggests that LaScO_3 and GdScO_3 syntheses indeed tend to result in higher $\text{Ln}(\text{OH})_3$ fractions and the lowest weight fraction of the desired phase.^{10,27} While the formation energy of LnOOH from the binary oxide does not vary widely with Ln, the formation energy of $\text{Ln}(\text{OH})_3$ demonstrates a clear trend. That trend is also observed in the energy of the reaction



which is shown in Figure 6b.

We can use this trend to inform our hydrosaua synthesis conditions. For those lanthanides with a stronger tendency to form $\text{Ln}(\text{OH})_3$, the optimal $P_{\text{H}_2\text{O}}$ for LnScO_3 formation will be lower by a factor proportional to the difference in $\text{Ln}(\text{OH})_3$ formation energy. Therefore, experimentally determining the optimal water-vapor partial pressure for one lanthanide scandate enables nearly phase-pure synthesis of the rest by following the trends expected from DFT. The water-vapor partial pressures used for the formation of all four lanthanide scandates are shown in Figure 6c. By adjusting $P_{\text{H}_2\text{O}}$ accordingly across the lanthanide series, we generate nearly phase-pure LnScO_3 nanoparticles for all four lanthanides tested, as can be seen in the PXRD patterns in Figure 7a. The morphology of the resulting LnScO_3 nanoparticles is shown in Figure 7b–d for Ln = Nd, Sm, and Gd. Contrary to those in Figure 4, LnScO_3 nanoparticles made under optimized conditions are well faceted and fairly uniform in shape and size.

The values of water-vapor partial pressure used to generate the results in Figure 7 are experimentally confirmed optimum

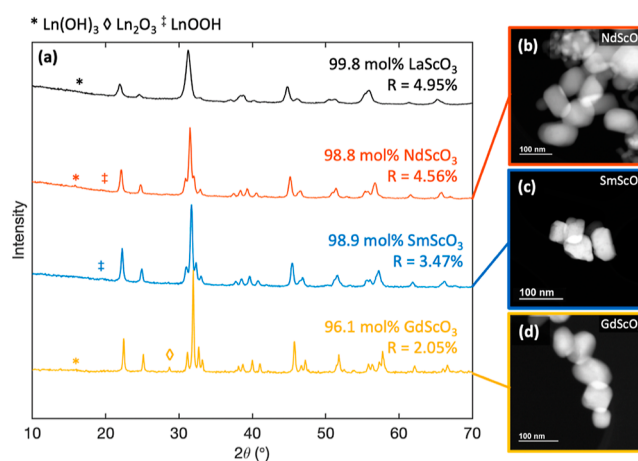


Figure 7. (a) PXRD patterns of LnScO_3 (Ln = La, Nd, Sm, Gd) obtained via two-line hydrosaua synthesis, adjusting $P_{\text{H}_2\text{O}}$ according to the trends calculated in Figure 6. (b–d) HAADF images of NdScO_3 , SmScO_3 , and GdScO_3 nanoparticles, respectively.

values. This phenomenon is demonstrated more explicitly in Figure 8. Conducting a hydrosaua synthesis of LnScO_3 with a water-vapor partial pressure lower than the appropriate value in Figure 6c results in smaller crystallite sizes or X-ray amorphous material, as shown by comparing Figure 8a,b. Using a higher water-vapor partial pressure results in significant $\text{Ln}(\text{OH})_3$ formation—shown by comparing Figure 8c,d—and, especially in the cases of Nd and Sm, the formation of LnOOH .

DISCUSSION

Reducing the partial pressure of water vapor by transitioning from a hydrothermal to a one-line hydrosaua approach was not sufficient to form phase-pure LnScO_3 for multiple lanthanides. As can be seen in Figure 4, the amount of water vapor in the synthesis environment will significantly affect the outcome. A two-line hydrosaua approach is needed to enable precisely controlled, very low water-vapor partial pressures. The diffraction patterns in Figure 7a further show that by adjusting the water-vapor partial pressure in accordance with thermodynamic trends across the lanthanide series, multiple LnScO_3 can be achieved with a high degree of phase purity. The trend in calculated reaction energy of eqs 2 and 3, shown in Figure 6, closely matches the trend in $P_{\text{H}_2\text{O}}$ that is required to synthesize LnScO_3 . Both trends essentially illustrate the water affinity of the lanthanides. $\text{La}(\text{OH})_3$ and $\text{Gd}(\text{OH})_3$, for

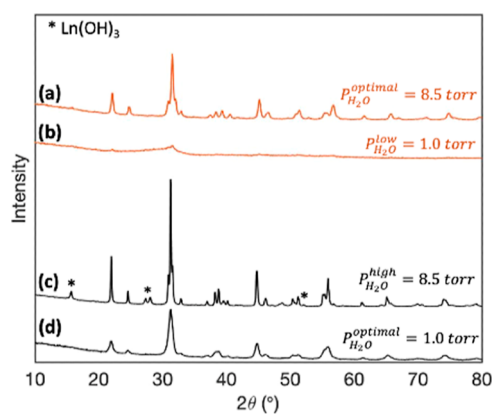


Figure 8. Red curves: PXRD patterns comparing NdScO_3 (a) synthesized at its optimal water-vapor partial pressure of 8.5 torr and (b) synthesized at a lower water partial pressure of 1.0 torr, with broader peaks resulting from smaller crystallite sizes. Black curves: PXRD patterns comparing LaScO_3 (c) synthesized at a higher-than-optimal water-vapor partial pressure of 8.5 torr, introducing $\text{La}(\text{OH})_3$, and (d) synthesized at its optimal water-vapor partial pressure of 1.0 torr.

example, are predicted to be more stable compounds than other $\text{Ln}(\text{OH})_3$ tested, which is consistent with experimental results in which the syntheses of LaScO_3 and GdScO_3 are more sensitive to excess water vapor. If we consider changing the water-vapor partial pressure from 3 to 10 torr at 725 K, this change corresponds to a change in water chemical potential of 7.25 kJ/mol. The increased chemical potential will have a greater effect when the driving force to form the hydroxide is small, for instance, in SmScO_3 , than it will when the driving force is large, for instance, in GdScO_3 . Thus, synthesizing GdScO_3 instead of $\text{Gd}(\text{OH})_3$ requires a larger decrease in the chemical potential of water. Both the reaction energies for $\text{Ln}(\text{OH})_3$ formation and the optimal $P_{\text{H}_2\text{O}}$ for LnScO_3 crystallization exhibit this trend. The correlation demonstrates

that, as hypothesized, water-vapor partial pressure is a crucial parameter to control phase purity in LnScO_3 hydrosynthesis.

We would like to point out that the electronic structure of the LnScO_3 gives us some insight into what causes energetic differences or differences in binding for various Ln. The partial density of states (pDOS) has been calculated for various bulk LnScO_3 and is shown in Figure 9. These pDOS indicate that Ln 4f states sit closer to the valence band edge for some LnScO_3 , for instance, NdScO_3 , than for others like GdScO_3 (this connects to the XPS in Figure 1). The pDOSs of some lanthanide scandates beyond those synthesized in this work (Ln = Pr, Pm, Eu, Tb) are also shown in Figure 9 to contextualize these results. The pDOS follows from the experimental XPS data shown in Figure 1. Compare, for instance, the sharp Pr 4f XPS peak in Figure 1a with the corresponding Pr 4f pDOS peak in Figure 9b. Similarly, Figure 1c illustrates GdScO_3 as having purely lower-lying 4f occupied states, consistent with the Gd 4f states lying further below the valence band edge in Figure 6g. The 4f electrons will therefore likely be more active in bonding in some Ln-containing compounds, such as PrScO_3 or NdScO_3 , than in others like GdScO_3 , forming one possible contribution to the non-monotonic thermodynamics of LnScO_3 formation.

While the trends calculated from DFT allow us to get a better handle on LnScO_3 , there are several factors that complicate our ability to determine an exact value of the true optimal $P_{\text{H}_2\text{O}}$ for each lanthanide. One must also consider the possibility of back-reactions: LnOOH formed during calcination may be reverted to $\text{Ln}(\text{OH})_3$ on cooling if $P_{\text{H}_2\text{O}}$ is still present. Given the evidence that LnOOH is more reactive and water-soluble than $\text{Ln}(\text{OH})_3$, and thus may more easily form the mixed-cation perovskite phase,^{13,28} hydrosynthesis was done using a two-step regime for water vapor: the appropriate DFT-predicted $P_{\text{H}_2\text{O}}$ was applied during the high-temperature (nucleation) calcination step and then lowered by

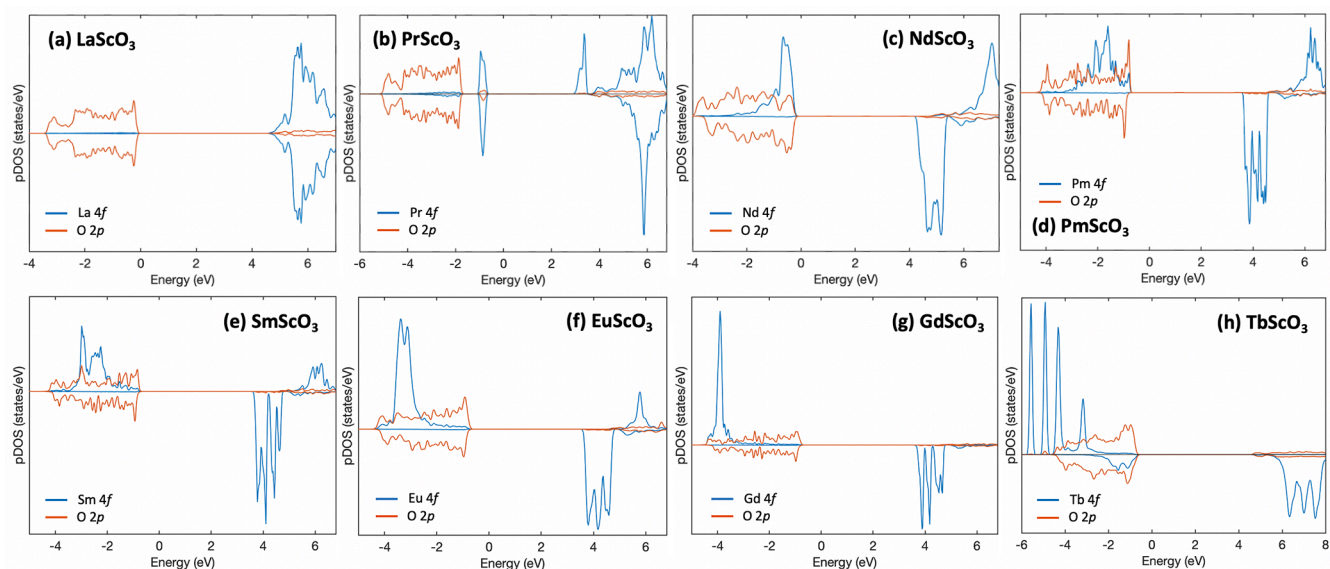


Figure 9. DFT-calculated pDOS of various bulk LnScO_3 . Red lines represent the oxygen 2p contribution, while the lanthanide 4f contribution is in blue. In (a) LaScO_3 , (f) EuScO_3 , and (g) GdScO_3 , the valence band edge consists largely of O 2p states, while in (b) and (c), the valence band edge is dominated by Pr 4f and Nd 4f states, respectively. The remaining (d) PmScO_3 , (e) SmScO_3 , and (h) TbScO_3 display a more intermediate mixture of Ln 4f and O 2p contributions at the valence band edge.

a factor of one-half before cooling down to the lower-temperature (growth) calcination step. By reducing $P_{\text{H}_2\text{O}}$ before cooling, we can prevent back-reactions from LnOOH to the more stable $\text{Ln}(\text{OH})_3$, resulting in a higher LnScO_3 weight fraction in the final product. The two-line hydrosaua reactor allows water-saturated air to be rapidly replaced by dry argon at the appropriate time.

Another factor to consider is the polymorphic and polyphasic nature of lanthanide sesquioxides, especially those with cations of intermediate sizes, such as Sm_2O_3 . While the hydrosaua synthesis method requires dissolution of these oxides in nitric acid, Ln_2O_3 is still occasionally present in the final product, for example, Gd_2O_3 in the GdScO_3 synthesis depicted in Figure 7a. It follows that either some Ln_2O_3 remains unreacted or new Ln_2O_3 is formed during calcination. DFT calculations were performed using the equilibrium polymorph of Ln_2O_3 below 2000 °C. For larger lanthanides, for example, sesquioxides La_2O_3 and Nd_2O_3 , their structure is hexagonal (A-type, space group $P6_3/mmm$); for smaller lanthanides as in Gd_2O_3 , the structure is cubic (C-type, space group $Ia\bar{3}$), and for intermediate size lanthanides as in Sm_2O_3 and Eu_2O_3 , the monoclinic structural form (B-type, space group $C2/m$) is most common.^{12,39–41} In reality, however, the Sm_2O_3 and Gd_2O_3 starting material will contain a polyphasic mixture of C- and B-type grains at room temperature. While polymorphism in the rare-earth sesquioxides has been studied extensively, the stability of certain phases and the exact nature of the polymorphic phase transitions $C \rightarrow B$ and $B \rightarrow A$ are still debated.^{41,42} Thus, because of the limitations of the ex situ techniques used in this work, it is difficult to say at what stage in the synthesis each phase is present. These phases may include unexpected Ln_2O_3 polymorphs or LnOOH that is formed but not seen in the final product due to rehydration to $\text{Ln}(\text{OH})_3$ on cooling.

These complicating factors tell us that there is more information to be gained about this system from in situ X-ray techniques. Variations among the four $\text{LnSc}(\text{OH})_6 \cdot x\text{H}_2\text{O}$ precursors prepared in this study, intermediate structures, or overall reaction mechanisms with varying Ln^{3+} could further corroborate the results of the previous section and explain more precisely the results shown in Figure 8 and the underlying differences responsible for the dependence on water-vapor partial pressure.

However, the PXRD results presented in Figure 7 demonstrate that the thermodynamic trends established herein are sufficient to guide hydrosaua synthesis of >96 mol % LnScO_3 for multiple lanthanides. By combining the two-line hydrosaua method with the thermodynamic trends calculated using DFT, the consistency of nearly phase-pure LnScO_3 synthesis is much improved. This approach should be generalizable to other oxide materials beyond the lanthanides as well; materials made hydrothermally from a hydrogel can likely be made with greater consistency and phase purity in large batches in a hydrosaua environment.

CONCLUSIONS

A mixed-cation hydroxide gel was calcined in a humid environment to produce various LnScO_3 . It was determined that water vapor is required to crystallize LnScO_3 particles with some control over their morphology but that too high a chemical potential of water will result in the formation of LnOOH and $\text{Ln}(\text{OH})_3$ at the expense of LnScO_3 . By

combining water-saturated and dry argon gas feeds, the humidity was greatly reduced and controlled. To determine the optimal water-vapor partial pressure as a function of lanthanide, DFT was used to calculate thermodynamic trends in LnOOH and $\text{Ln}(\text{OH})_3$ formation from water and Ln_2O_3 . These trends served as a guide to the required water-vapor partial pressure for each lanthanide, resulting in enhanced LnScO_3 phase purity and consistency of results. This approach may be general to other complex oxides as a route to consistent and scalable open-system synthesis.

AUTHOR INFORMATION

Corresponding Author

Emily P. Greenstein – Department of Materials Science & Engineering, Northwestern University, Evanston, Illinois 60208, United States; orcid.org/0000-0002-3394-9808; Email: emilygreenstein@u.northwestern.edu

Authors

Kenneth R. Poeppelmeier – Department of Chemistry, Northwestern University, Evanston, Illinois 60208, United States; orcid.org/0000-0003-1655-9127

Laurence D. Marks – Department of Materials Science & Engineering, Northwestern University, Evanston, Illinois 60208, United States; orcid.org/0000-0002-6659-2016

Complete contact information is available at:

<https://pubs.acs.org/10.1021/acs.inorgchem.2c04107>

Author Contributions

The manuscript was written through the contributions of all authors. All authors have given approval to the final version of the manuscript.

Notes

The authors declare no competing financial interest.

ACKNOWLEDGMENTS

This work was supported by the Northwestern University Institute for Catalysis in Energy Processes (ICEP) under grant no. DOE DE-FG02-03ER15457. ICEP is funded by the Chemical Sciences, Geosciences, and Biosciences Division, Office of Science, U.S. Department of Energy. The authors acknowledge Dr. Robert Kennedy and Dr. Fenghua Ding for their help to design and construct the hydrosaua reactor, and Dr. Ryan Paull for his discussions about and fundamental contributions to development of the hydrosaua method.

REFERENCES

- (1) Darr, J. A.; Zhang, J.; Makwana, N. M.; Weng, X. Continuous Hydrothermal Synthesis of Inorganic Nanoparticles: Applications and Future Directions. *Chem. Rev.* **2017**, *117*, 11125–11238.
- (2) Canu, G.; Buscaglia, V. Hydrothermal synthesis of strontium titanate: thermodynamic considerations, morphology control and crystallisation mechanisms. *CrystEngComm* **2017**, *19*, 3867–3891.
- (3) Rabuffetti, F. A.; Kim, H.-S.; Enterkin, J. A.; Wang, Y.; Lanier, C. H.; Marks, L. D.; Poeppelmeier, K. R.; Stair, P. C. Synthesis-Dependent First-Order Raman Scattering in SrTiO_3 Nanocubes at Room Temperature. *Chem. Mater.* **2008**, *20*, 5628–5635.
- (4) Dong, L.; Shi, H.; Cheng, K.; Wang, Q.; Weng, W.; Han, W. Shape-controlled growth of SrTiO_3 polyhedral submicro/nanocrystals. *Nano Res.* **2014**, *7*, 1311–1318.
- (5) Walters, L. N.; Wang, E. L.; Rondinelli, J. M. Thermodynamic Descriptors to Predict Oxide Formation in Aqueous Solutions. *J. Phys. Chem. Lett.* **2022**, *13*, 6236–6243.

- (6) Lencka, M. M.; Riman, R. E. Thermodynamic Modeling of Hydrothermal Synthesis of Ceramic Powders. *Chem. Mater.* **1993**, *5*, 61–70.
- (7) Talapatra, A.; Ueberuga, B. P.; Stanek, C. R.; Pilania, G. A Machine Learning Approach for the Prediction of Formability and Thermodynamic Stability of Single and Double Perovskite Oxides. *Chem. Mater.* **2021**, *33*, 845–858.
- (8) Raccuglia, P.; Elbert, K. C.; Adler, P. D.; Falk, C.; Wenny, M. B.; Mollo, A.; Zeller, M.; Friedler, S. A.; Schrier, J.; Norquist, A. J. Machine-learning-assisted materials discovery using failed experiments. *Nature* **2016**, *533*, 73–76.
- (9) Uecker, R.; Velickov, B.; Klimm, D.; Bertram, R.; Bernhagen, M.; Rabe, M.; Albrecht, M.; Fornari, R.; Schlom, D. G. Properties of rare-earth scandate single crystals (Re=Nd–Dy). *J. Cryst. Growth* **2008**, *310*, 2649–2658.
- (10) Paull, R. J.; Ly, T.; Mansley, Z. R.; Poepfelmeier, K. R.; Marks, L. D. Controlled Two-Step Formation of Faceted Perovskite Rare-Earth Scandate Nanoparticles. *Crystals* **2019**, *9*(). DOI: 10.3390/cryst9040218
- (11) Mansley, Z. R.; Paull, R. J.; Saveriede, L.; Tatro, S.; Greenstein, E. P.; Gosavi, A.; Cheng, E.; Wen, J.; Poepfelmeier, K. R.; Notestein, J. M.; Marks, L. D. Identifying Support Effects in Au-Catalyzed CO Oxidation. *ACS Catal.* **2021**, *11*, 11921–11928.
- (12) Adachi, G.; Imanaka, N.; Kang, Z. C., Eds. In *Binary Rare Earth Oxides*; Kluwer Academic: Dordrecht, 2004.
- (13) Stampfer, E. S.; Sheets, W. C.; Prellier, W.; Marks, T. J.; Poepfelmeier, K. R. Hydrothermal synthesis of LnMnO₃ (Ln = Ho–Lu and Y): exploiting amphotericism in late rare-earth oxides. *J. Mater. Chem.* **2009**, *19*, 4375.
- (14) Liferovich, R. P.; Mitchell, R. H. A structural study of ternary lanthanide orthoscatate perovskites. *J. Solid State Chem.* **2004**, *177*, 2188–2197.
- (15) Jin, G. B.; Choi, E. S.; Albrecht-Schmitt, T. E. Syntheses, structures, magnetism, and optical properties of gadolinium scandium chalcogenides. *J. Solid State Chem.* **2009**, *182*, 1075–1081.
- (16) Mansley, Z. R.; Mizzi, C. A.; Koirala, P.; Wen, J.; Marks, L. D. Structure of the (110) LnScO₃ (Ln = Gd, Tb, Dy) surfaces. *Phys Rev Mater* **2020**, *4*, 045003.
- (17) Mizzi, C. A.; Koirala, P.; Marks, L. D. Electronic structure of lanthanide scandates. *Phys Rev Mater* **2018**, *2*, 025001.
- (18) Mansley, Z. R.; Paull, R. J.; Greenstein, E. P.; Wen, J. G.; Poepfelmeier, K. R.; Marks, L. D. ScOx rich surface terminations on lanthanide scandate nanoparticles. *Phys Rev Mater* **2021**, *5*(). DOI: 10.1103/physrevmaterials.5.125002
- (19) Jeong, N. C.; Lee, J. S.; Tae, E. L.; Lee, Y. J.; Yoon, K. B. Acidity scale for metal oxides and Sanderson's electronegativities of lanthanide elements. *Angew Chem Int Ed Engl* **2008**, *47*, 10128–10132.
- (20) Gagne, O. C.; Hawthorne, F. C. Empirical Lewis acid strengths for 135 cations bonded to oxygen. *Acta Crystallogr B Struct Sci Cryst Eng Mater* **2017**, *73*, 956–961.
- (21) Haasch, R. T.; Martin, L. W.; Breckenfeld, E. Single Crystal Rare-earth Scandate Perovskites Analyzed Using X-ray Photoelectron Spectroscopy: 1. PrScO₃(110). *Surf. Sci. Spectra* **2014**, *21*, 131–139.
- (22) Haasch, R. T.; Martin, L. W.; Breckenfeld, E. Single Crystal Rare-earth Scandate Perovskites Analyzed Using X-ray Photoelectron Spectroscopy: 2. NdScO₃(110). *Surf. Sci. Spectra* **2014**, *21*, 140–148.
- (23) Haasch, R. T.; Martin, L. W.; Breckenfeld, E. Single Crystal Rare-earth Scandate Perovskites Analyzed Using X-ray Photoelectron Spectroscopy: 3. GdScO₃(110). *Surf. Sci. Spectra* **2014**, *21*, 149–156.
- (24) Haasch, R. T.; Martin, L. W.; Breckenfeld, E. Single Crystal Rare-earth Scandate Perovskites Analyzed Using X-ray Photoelectron Spectroscopy: 4. TbScO₃(110). *Surf. Sci. Spectra* **2014**, *21*, 157–164.
- (25) Haasch, R. T.; Martin, L. W.; Breckenfeld, E. Single Crystal Rare-earth Scandate Perovskites Analyzed Using X-ray Photoelectron Spectroscopy: 5. DyScO₃(110). *Surf. Sci. Spectra* **2014**, *21*, 165–172.
- (26) Zhang, Y. Electronegativities of Elements in Valence States and Their Applications. 2. A Scale for Strengths of Lewis Acids. *Inorg. Chem.* **1982**, *21*, 3889–3893.
- (27) Paull, R. J.; Mansley, Z. R.; Ly, T.; Marks, L. D.; Poepfelmeier, K. R. Synthesis of Gadolinium Scandate from a Hydroxide Hydrogel. *Inorg. Chem.* **2018**, *57*, 4104–4108.
- (28) Marshall, K. P.; Blichfeld, A. B.; Skjærø, S. L.; Grendal, O. G.; Beek, W.; Selbach, S. M.; Grande, T.; Einarsrud, M. A. A Fast, Low-Temperature Synthesis Method for Hexagonal YMnO₃: Kinetics, Purity, Size and Shape as Studied by In Situ X-ray Diffraction. *Chemistry* **2020**, *26*, 9330–9337.
- (29) Shafer, M. W.; Roy, R. Rare-Earth Polymorphism and Phase Equilibria in Rare-Earth Oxide-Water Systems. *J. Am. Ceram. Soc.* **1959**, *42*, 563–570.
- (30) Ali, F.; Smith, M. E.; Steuermagel, S.; Whitfield, H. J. ¹⁷O solid-state NMR examination of La₂O₃ formation. *J. Mater. Chem.* **1996**, *6*, 261–264.
- (31) Raekers, M.; Kuepper, K.; Bartkowski, S.; Prinz, M.; Postnikov, A. V.; Potzger, K.; Zhou, S.; Arulraj, A.; Stüßler, N.; Uecker, R.; Yang, W. L.; Neumann, M. Electronic and magnetic structure of RScO₃ (R=Sm,Gd,Dy) from x-ray spectroscopies and first-principles calculations. *Phys. Rev. B* **2009**, *79*, 125114.
- (32) Haasch, R. T.; Breckenfeld, E.; Martin, L. W. An Introduction to Single Crystal Perovskites and Single Crystal Rare-Earth Scandate Perovskites Analyzed Using X-ray Photoelectron Spectroscopy. *Surf. Sci. Spectra* **2014**, *21*, 84–86.
- (33) Stevie, F. A.; Donley, C. L. Introduction to x-ray photoelectron spectroscopy. *J. Vac. Sci. Technol., A* **2020**, *38*(). DOI: 10.1116/6.0000412
- (34) Yeh, J. J.; Lindau, I. Atomic Subshell Photoionization Cross Sections and Asymmetry Parameters: 1 < Z < 103. *Atomic Data and Nuclear Data Tables* **1985**, *32*, 1–155.
- (35) Novák, P.; Kuneš, J.; Chaput, L.; Pickett, W. E. Exact exchange for correlated electrons. *Phys. Status Solidi B* **2006**, *243*, 563–572.
- (36) Blaha, P.; Schwarz, K.; Tran, F.; Laskowski, R.; Madsen, G. K. H.; Marks, L. D. WIEN2k: An APW+lo program for calculating the properties of solids. *J. Chem. Phys.* **2020**, *152*, 074101.
- (37) Perdew, J. P.; Ruzsinszky, A.; Csonka, G. I.; Vydrov, O. A.; Scuseria, G. E.; Constantin, L. A.; Zhou, X.; Burke, K. Restoring the Density-Gradient Expansion for Exchange in Solids and Surfaces. *Phys. Rev. Lett.* **2008**, *100*(). DOI: 10.1103/PhysRevLett.100.136406
- (38) Veličkov, B.; Kahlenberg, V.; Bertram, R.; Bernhagen, M. Crystal chemistry of GdScO₃, DyScO₃, SmScO₃ and NdScO₃. *Zeitschrift für Kristallographie* **2007**, *222*, 466–473.
- (39) Saiki, A.; Ishizawa, N.; Nobuyasu, M.; Kato, M. Structural change of C-rare earth sesquioxides Yb₂O₃ and Er₂O₃ as a function of temperature. *Yogyo Kyokai-Shi* **1985**, *93*, 649–654.
- (40) Schleid, T.; Meyer, G. Single crystals of rare earth oxides from reducing halide melts. *J. Less-Common Met.* **1989**, *149*, 73–80.
- (41) Artini, C.; Pani, M.; Plaisier, J. R.; Costa, G. A. Structural study of Nd oxidation by means of in-situ synchrotron X-ray diffraction (400 ≤ T ≤ 700 °C). *Solid State Ionics* **2014**, *257*, 38–41.
- (42) Zinkevich, M. Thermodynamics of rare earth sesquioxides. *Prog. Mater. Sci.* **2007**, *52*, 597–647.